Thermospheric Variations From GNSS and Accelerometer Measurements on Small Satellites

This paper presents an overview of past and present developments and efforts in sensing and modeling thermospheric density, wind variations, as well as future challenges and perspectives for GNSS and accelerometers on small satellites.

By Shuanggen Jin ⓘ, Andres Calabia, *Member IEEE*, and Liangliang Yuan

ABSTRACT | Monitoring and understanding geophysical processes in the thermosphere is primordial for space physics, low Earth orbiters, and ground-based technologies. In the last half century, thermospheric variations, anomalies, and climatology have been investigated and reported, but were limited due to lack of observations and large uncertainty in the models. Today, Global Navigation Satellite Systems (GNSS) and accelerometers on small satellites can sense neutral-density and wind variations with unprecedented accuracy, which contribute to understand thermospheric variations and improve the current empirical and physical models. In this paper, an overview of past and present developments and efforts in sensing and modeling thermospheric density and wind variations is presented, as well as the future challenges and perspectives for GNSS and accelerometers on small satellites.

KEYWORDS | Accelerometer; Global Navigation Satellite System (GNSS); small satellites; thermosphere

I. INTRODUCTION

The top layer of the atmosphere is highly variable in space and time, and its physical processes are very complex. The thermosphere is the layer above 85-km height, where the photoabsorption, photoionization, and photodissociation of molecules through extreme ultraviolet radiation (EUV) create the ions of the ionosphere. Above 160 km, the neutral density is too low for molecular interaction, and the regular dynamics are mainly driven by the day–night heating, the annual cycles, and transferring thermal energy from ions to neutrals. Variations in energy exchange produced by, e.g., solar flux variations, produce the expansion/contraction of the thermosphere, and the consequent changes of density at a given altitude. In addition, the solar wind plasma, combined with a favorable alignment of the interplanetary magnetic field, produce thermospheric Joule heating and particle precipitation along the Earth's magnetic field lines. These processes create additional variations in the thermospheric mass density distribution. Coronal mass ejections (CMEs) and geomagnetic storms are generally abrupt short-term changes in comparison with diurnal and annual variations.

Previous studies have shown the existing coupling between the thermosphere and the ionosphere [1], and the repercussions on human activity. For instance, the practical importance of the ionosphere in radio propagation [2]–[5], or the damaging effects of geomagnetic storms and CME on orbiting and ground-based technologies [6]–[9] are well known. Currently, half of the world's active satellites operate in low Earth orbit (LEO),

ranging from altitudes of 160–2000 km. At low altitudes, atmospheric drag is the major cause of orbital decay and perturbations, limiting the lifetime of the satellite missions. The accurate prediction of precise orbital ephemeris (POE) in precise orbit determination (POD) is the result of an integrated knowledge of atmospheric density and space weather, where the force models provide the inputs for a mission lifetime [10]. Thus, it is clear that accurate air density models are essential for the upper-atmosphere research and applications. However, in view of the highly expected accuracy from the present and future LEO POD products, the current thermospheric air density models are unable to predict the variability as accurately and efficiently required.

During the last half century, the use of accelerometers to derive termospheric density and wind estimates has been providing an unprecedented detail in sensing the global distribution, climatology, and variations [11]. The technique is based on removing accurate radiation pressure models from measured nongravitational accelerations, and then to use the drag-force formula to compute density and wind estimates [12]–[13]. In addition, several studies have recently shown that nongravitational accelerations can be estimated through GPS-based POD of LEO [14]–[17]. Undoubtedly, GPS-based POD of LEO for thermospheric density and wind estimation is a promising source of observables. With the increasing number of small satellites being equipped with a high-precision Global Navigation Satellite System (GNSS) receivers, accelerometers, and more enhanced data processing and orbit determination strategies, drag-derived density and wind products promise potentially good applications for the thermospheric research community, e.g., coming Constellation Observing System for Meteorology, Ionosphere, and Climate (COSMIC)-2 with 12 satellites.

The aim of this paper is to review the past and present status on thermospheric mass density and wind variations. Recent developments and results on thermospheric mass density and wind variations from GNSS and accelerometer measurements are presented. Finally, future challenges and perspective on small satellites are given and discussed.

II. THERMOSPHERE MODELS

The first thermosphere density models were based on orbital decay of satellites, and started in the 1960s by Harris and Priester [18] and Jacchia [19]. Along time, Jacchia models have been improved with the use of new algorithms and proxies [20]. Afterwards, the first series of the drag temperature model (DTM) were based on observations of satellite drag and neutral atmospheric temperatures [21]. Currently, DTM incorporates accelerometer, mass spectrometer, incoherent scatter radar, and optical airglow measurements [22]. The mass spectrometer and incoherent scatter (MSIS) radar series of models were originally based on mass spectrometer and incoherent scatter radar observations [23]. While the mathematical formulations of MSIS and DTM use the exponential Bates profile [24], the Jacchia series use the arctangent function to
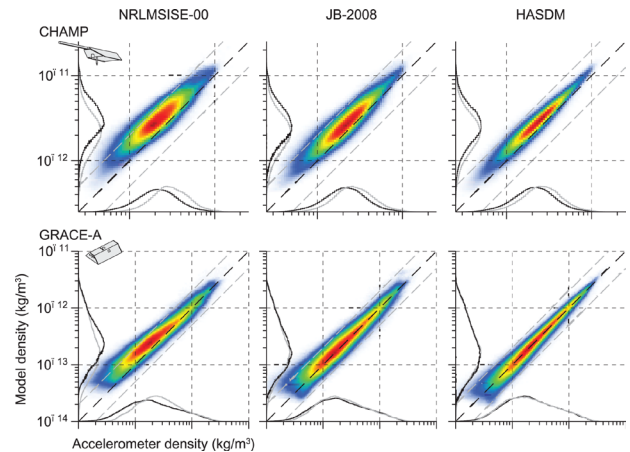

Fig. 1. *The distribution of CHAMP and GRACE-A densities, with their equivalent model densities for MSIS (NRLMSISE-00), Jacchia (JB-2008), and HASDM. The line graphs at both axes show simple 2-D histograms of their corresponding data set in black [13].*

represent an asymptotic behavior for the upper thermosphere. Today, MSIS is the standard for international space research, and the current release (NRLMSISE-00) has been updated with satellite drag data and solar ultraviolet (UV) occultation [25]. The parameters of temperature and density of MSIS depend on solar flux and geomagnetic indices, which are modulated in longitude, latitude, and local solar time (LST) variations. Fig. 1 pictures the histograms of the Gravity Recovery and Climate Experiment (GRACE) and the Challenging Minisatellite Payload (CHAMP) data versus MSIS, Jacchia, and the high-accuracy satellite drag model (HASDM). In this figure, the best match is pictured by HASDM, showing its data cloud better distributed along the diagonal.

Additional thermospheric models have been developed with the finality to accurately represent the climatologically thermospheric density variations, e.g., the accelerometer density model (ADM) of Marcos *et al.* [26], the global average mass density model (GAMDM) of Emmert [27], CHAMP-based model of Liu *et al.* [28], or the parameterized principal component analysis (PCA) of GRACE densities in [29]. Due to the lack of *in situ* and remote sensing observations in between 120- and 400-km altitude, Oberheide *et al.* [30] developed the climatological tidal model of the thermosphere (CTMT) based on temperature and wind observations. They used the Hough mode extension to extrapolate the model of mesosphere/lower thermosphere into the thermosphere. Unfortunately, poor agreements were found with CHAMP observations.

The HWM07 horizontal wind model [31] is a statistical representation from the ground to the exosphere, based on gradient winds from the Committee on Space Research International Reference Atmosphere (CIRA-86) plus rocket soundings, incoherent scatter radar, medium-frequency radar, and meteor radar data. His predecessors were HWM93, HWM90, and HWM87 [32]. HWM07 can represent both quiet and disturbed geomagnetic conditions,

and the parameterization of solar activity is planned to be included in future versions. A recent update (HWM14) provides an improved time-dependent, observationally based, global empirical specification of the upper atmospheric general circulation patterns and migrating tides [33]. Physical models generally use empirical parameterizations and boundary conditions to solve fluid equations. Detailed descriptions for physical models are given in the review of Emmert [27] and Akmaev [34]. Compared to empirical models, physical models require more expert knowledge and, therefore, are more suitable for scientific investigations than for routine applications, e.g., orbit determination.

The thermosphere–ionosphere–electrodynamics general circulation model (TIE-GCM) [35]–[36] solves 3-D fluid equations for the mutual diffusion of N_2, O_2, and O. Including a coupled ionosphere, reactions in TIE-GCM involve ion species and energy budget, as well as self-consistent generation of middle and low latitude electric fields by neutral winds. Kim *et al.* [37] incorporated NRLMSISE-00 partial pressures of He into TIE-GCM, contributing to variations in mass density, specific heat, viscosity, and thermal conductivity. Hagan *et al.* [38] attempted to extend the global-scale wave model (GSWM) with migrating solar tides, using the TIE-GCM to calculate the neutral gas heating that dominates the forces from solar activities. The main idea was to confirm whether the model fitted the seasonal characteristics and the solar cycle variability. Diurnal temperature amplitude did vary with solar activity while there was no corresponding wind caused by solar cycle variability. The new GSWM showed a good consistency with the TIE-GCM results. Häusler *et al.* [39] proposed a new boundary scheme in TIE-GCM based on NASA Modern Era Retrospective-Analysis for Research and Applications (MERRA) temperature, in which self-consistently could explain the day-to-day tidal and planetary wave variability. The model showed a more variable and complicated pattern especially of the neutral temperature. The nonmigrating tide in the lower boundary scheme TIE-GCM/MERRA was larger than that in TIE-GCM/GSWM, causing stronger vertical atmospheric transport. The authors pointed out that stronger vertical transport leads to a smaller density due to the compositional mixing effect dominated by the atomic oxygen. Aside from these two models based on the TIE-GCM framework, thermosphere, ionosphere, mesosphere energetics, and dynamics (TIMED) also can explain temperature variations.

III. THERMOSPHERIC DENSITY AND WIND ESTIMATION

A. Theory and Methods

Besides pressure gauge [40] and neutral mass spectrometry [41]–[42], the analysis of satellite orbital decay through the Gauss's form of Lagrange's planetary equations (perturbation equations) has been the basis to derive thermospheric mass densities since 1958 [43]. By determining the time

derivatives of the energy and the angular momentum of an orbiting object over time [44], the equations of King-Hele [45] showed that the primary effect of drag acceleration is to monotonically reduce the orbital semimajor axis. Thus, by only measuring discrete changes in the magnitude of the semimajor axis, the corresponding density averages along the trajectory of a LEO object can be derived with temporal resolution from hours to days [46]–[48].

In the POD process, the position and velocity of an orbiting object is statistically estimated by a set of equations of motion and a set of discrete observations [49]. Currently, the most precise techniques for orbital tracking include satellite-to-satellite GNSS, satellite laser ranging (SLR), and Doppler orbitography and radiopositioning integrated by satellite (DORIS). The tree main approaches currently used in POD are the dynamic, kinematic, and reduced-dynamic schemes. In the dynamic approach, the measurements determine the state of the satellite (position and velocity) at some initial epoch, and then the solution is mapped forward in time using the dynamical models. In the kinematic approach, the state of the satellite is determined sequentially at each observational measurement, and without dependence on the dynamical models. The last is the reduced-dynamic approach, where the parameters to solve for the dynamic models are fixed when a solution is obtained, and with additional accelerations estimated from the observational measurements [50]. The reduced-dynamic approach is the most complete and accurate strategy because the combination of high-precision GNSS observables with the dynamical models (e.g., time-variable gravity-field, nongravitational force models) counterbalance both the disadvantages of the GNSS measurement noises and the uncertainties in the models.

The main external forces to account in a POD strategy include gravitational forces, atmospheric drag, and irradiative pressure (Fig. 2). Basically, the three main sources of
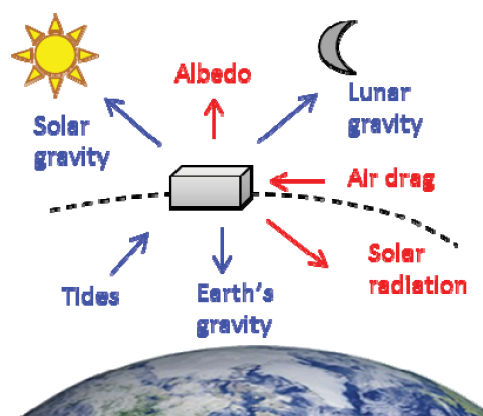

Fig. 2. *Accelerations acting on a satellite. Gravitational accelerations are pictured in blue, and nongravitational in red. Nongravitational accelerations are derived from POE in the POD process. The acceleration we finally need to derive the thermospheric density is the "air drag" acceleration.*
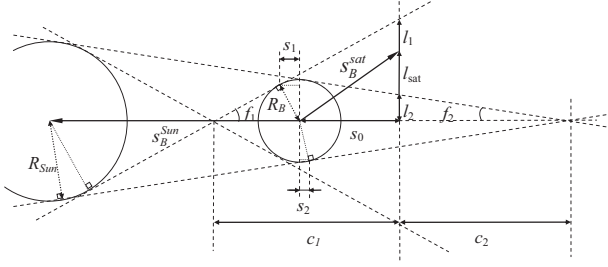
Fig. 3. *Eclipse computation geometry: if l_{sat} is bigger than l_2 and smaller than l_1, and s_0 is bigger than s_1, the spacecraft is in penumbra (sh = fg). Otherwise, if s_0 is bigger than s_2 and l_{sat} is smaller than l_2, the spacecraft is umbra (sh = O). For the rest of cases, the spacecraft is in sunlight (sh = 1).*

Fig. 4. *Induced direct solar radiation acceleration for GRACE-A in the SBS on April 1, 2005.*

irradiative accelerations are the direct solar radiation pressure, the reflected solar radiation pressure (albedo), and the terrestrial infrared radiation. While the terrestrial infrared radiation is almost independent from illumination conditions, the direct and the reflected solar radiations must be multiplied by a ratio to account for planetary eclipses [51]. Fig. 3 depicts the eclipse geometry for an accurate computation, where the International Terrestrial Reference System (ITRS) coordinates of the Sun (Sun) and the spacecraft (sat) are calculated with respect to the occulting body B (for each case, B = moon, Earth). Note that for Earth, $r_{Earth} = 0$. Then, the fundamental plane (plane perpendicular to the shadow axis and passes through the satellite) intersects the shadow axis at a distance $s_0 = (- s_B^{sat} \times s_B^{Sun})/s_B^{Sun}$, and the distances needed to compute the shadow algorithm are obtained [51].

When the spacecraft is in penumbra, a fractional area of the solar disc that is blocked by the occulting body can be applied to the incoming solar flux ($sh = fg$). Using the circumflex mark as for denoting unit vectors, the closest point to the Earth on the Sun–satellite vector s_{Sun}^{sat} is

$$r_p = r_{sat} - \left(\hat{s}_{Sun}^{sat} \cdot r_{sat} \right) \hat{s}_{Sun}^{sat}. \tag{1}$$

The apparent radius of the solar disc projected on a plane through this point, perpendicular to the satellite–Sun vector is

$$R_{Sun}^{'} = \frac{\left\| \left(\hat{s}_{Sun}^{sat} \cdot r_{sat} \right) \hat{s}_{Sun}^{sat} \right\|}{s_{Sun}^{sat}} R_{Sun}^{'}$$

$$\eta = \frac{r_p - R_{Earth}}{R_{Sun}^{'}} \delta_{sh, penumbra}$$

$$f_g = 1 - \frac{1}{\pi} \arccos(\eta) + \sqrt{1 - \eta^2} \tag{2}$$

where $\delta_{j,k}$ is the Kronecker's delta. On the plates of the user's satellite, one part of the incoming radiation is absorbed and the other is reflected diffusely and specularly. The equation to determine the entire resultant force on the satellite due to solar radiation accounts for the plate areas and
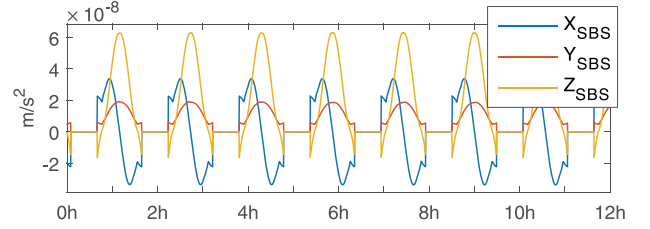
their orientation, their coefficients of diffusive and specular reflectivity, and the mass of the satellite [52]

$$a_{sr} = \sum_{i=1}^{n_p} - \frac{E_{sr} A_i \hat{n}_i \cdot \hat{s}_{Sun}^{sat}}{mc}$$

$$\times \left[2 \left(\frac{c_{rd,i}}{3} + c_{rs,i} \hat{n}_i \times \hat{s}_{Sun}^{sat} \right) \hat{n}_i + (1 - c_{rs,i}) \hat{s}_{Sun}^{sat} \right] \tag{3}$$

where n_p is the number of plates, A_i is the plate area, c is the speed of light, $c_{rd,i}$ is the coefficient of diffusive reflectivity, $c_{rs,i}$ is the coefficient of specular reflectivity, m is the satellite mass, $\hat{n}_i$ is the unit plate normal, $\hat{s}_{Sun}^{sat}$ is the unit Sun–satellite vector, and $E_{sr} = sh \cdot 1366 (1AU/ s_{Sun}^{sat})^2$ is the flux on the Earth's atmosphere (1366 W/m^2), corrected from the yearly period of the Earth's orbit eccentricity and from the planetary eclipse ratio sh. Fig. 4 shows the resulting solar radiation acceleration for GRACE in the satellite body system (SBS) on April 1, 2005. Note in SBS, the X_{SBS}-axis is the long axis of symmetry of the satellite, pointing in the direction of the K-band ranging (KBR) phase center, the Y_{SBS}-axis is the vertical axis of symmetry, and the Z_{SBS}-axis completes the right-handed coordinate system.

In a similar way, the Earth albedo must be computed accounting for the reflected solar radiation and the terrestrial infrared radiation

$$a_{ea} = \sum_{i=1}^{n_p} \sum_{j=1}^{grid} - \frac{E_{ea,j} A_i \hat{n}_i \cdot \hat{s}_j^{sat}}{mc}$$

$$\times \left[2 \left(\frac{c_{rd,i}}{3} + c_{rs,i} \hat{n}_i \times \hat{s}_j^{sat} \right) \hat{n}_i + (1 - c_{rs,i}) \hat{s}_j^{sat} \right] \tag{4}$$

where the parameter $E_{ea,j} = E_{ea}^R + E_{ea}^{IR}$ is composed of shortwave E_{ea}^R and long-wave E_{ea}^{IR} radiation.

For the terrestrial infrared radiation, Knocke and Ries [53] modeled the seasonal and latitudinal variations of a black body with a surface temperature of 288 °K. The reflected radiant flux is a fraction of the incoming flux, and can be computed from the reflectivity index, which is measured, e.g., by the Total Ozone Mapping Spectrometer (TOMS) mission. Detailed algorithms to remove irradiative accelerations can be found, e.g., in [13] and [54]. Fig. 5 shows the resulting terrestrial infrared radiation acceleration and Earth albedo acceleration for GRACE in the SBS on April 1, 2005.

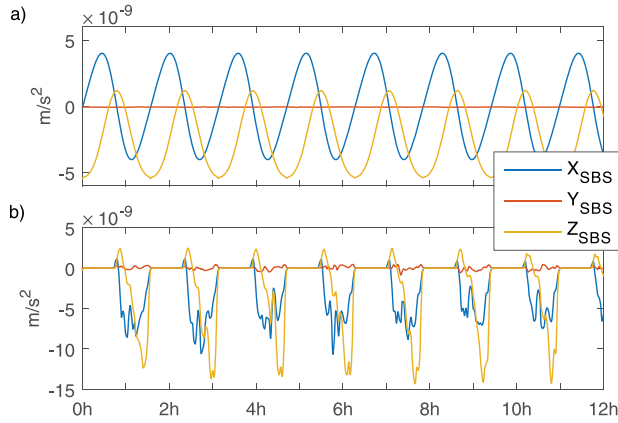Finally, radiative accelerations are removed from nongravitational accelerations, and the resulting force is the

Fig. 5. *(a) Induced terrestrial infrared radiation acceleration and (b) Earth albedo acceleration for GRACE-A in the SBS on April 1, 2005.*

combined effect of atmospheric drag and wind (aerodynamic), and can be expressed as a dynamic pressure applied on a reference area

$$F_a = \frac{1}{2} CA\rho v_r^2 \qquad (5)$$

where ρ is the atmospheric mass density, C is the drag coefficient vector, and A is the cross-sectional area perpendicular to the relative velocity of the atmosphere with respect to the spacecraft (v_r). In this equation, the dimensionless drag coefficient C is required to represent the interaction between the satellite and the flow. Most of satellites flow in the regime of high vacuum (flow can be considered to be individual particles moving in straight lines), and several analytical methods have been developed to represent the free molecular flow [55], [56]. Simplified assumptions to Schamberg's formulas, where the drag coefficient vector C is decomposed in drag C_D and lift C_L for each plate i are given by Cook [57]

$$C_{Li} = \frac{4}{3}\sqrt{1 + \alpha_i\left(\frac{T_{w,i}}{T_a} - 1\right)} \sin \theta_i$$

$$C_{Di} = 2 + \frac{4}{3}\sqrt{1 + \alpha_i\left(\frac{T_{w,i}}{T_a} - 1\right)} \cos \theta_i \qquad (6)$$

where T_a is the temperature of the atmosphere (e.g., from a thermospheric model), $T_{w,i}$ is the surface temperature of plate i, Θ_i is the angle of incident gas flow with respect to the plate, and α_i is the high-speed substrate material accommodation coefficient [58]

$$\alpha_i = \frac{3.6\,\mu_i}{(1 + \mu_i)^2}. \qquad (7)$$

The molecular mass ratio μ can be obtained from the mean molecular density of the atmosphere divided by the molecular density of each plate. The mean molecular density (g/mol) of the atmosphere can be obtained from the sum of partial number densities (m^{-3}), multiplied by their atomic

mass, and divided by the total volume. Values from an atmospheric model can be employed for calculations.

Unfortunately, the free molecular closed-form solutions cannot accurately account for multiple reflections, and new computational methods are being developed to compute physical drag coefficients [59]. These methods can include, e.g., direct simulation Monte Carlo (DSMC) simulations or the test particle modeling. For instance, physical drag coefficients computed using different gas–surface interaction models are compared in [60].

Several approaches and simplifications for density estimation [see (7)] can be found in [13], including the projection of the aerodynamic acceleration on the relative velocity (drag), and the projection of drag on the inertial velocity. These approximations allow assuming that the drag acceleration vector is coplanar with the orbital plane, and the in-plane perturbation equations from celestial mechanics can therefore be applied. Finally, after solving the drag-force equation for the densities at each satellite position, the derived values can be normalized to a common height (h) following the indications of Rentz and Lühr [61]

$$\rho(475\ \text{km}) = \rho_{\text{obs}}(h)\frac{\rho_{\text{model}}(475\ \text{km})}{\rho_{\text{model}}(h)}. \qquad (8)$$

In LEO, the errors caused by the normalization of changes in altitude of ~100 km are expected to be small enough (within 5%), as discussed in [62].

B. Thermospheric Estimation From Accelerometers

During this current era of LEO and space/planetary exploration, geodetic small satellites are continuously evolving, and several scientific missions are providing a wide range of measurement types. Besides the onboard GNSS receivers and satellite laser ranging (SLR) reflectors, other several instruments can be employed to improve the accuracy of the POD and related products [63]–[64]. For instance, accelerometers on LEO satellites are being used to measure the nongravitational accelerations needed in the POD process. In addition, equaling the drag-force formula to accelerometer-derived aerodynamic accelerations is currently providing an unprecedented detail and accuracy in thermospheric neutral densities and cross-track winds retrieval [12], [13], [15]. The principle of a satellite accelerometer is based on measuring the force needed to keep a proof mass exactly at the spacecraft's center of mass, where the gravity is exactly compensated by the centrifugal force. Plus and minus drive voltages are applied to electrodes with respect to opposite sides of the proof mass, whose electrical potential is maintained at a direct current (dc) biasing voltage.

The first satellite accelerometers were flown in 1968 with thermospheric-modeling purposes, e.g., Miniature Electrostatic Single-axis Accelerometer (MESA), Satellite Electrostatic Triaxial Accelerometer (SETA), and CACTUS

(French acronym meaning ultrasensitive, three-axis, capacitive accelerometric transducer). Unfortunately, the sparse spatiotemporal distribution of measurements limited the resulting scientific research, products, and models. Today, the CHAMP, GRACE, and Gravity Field and Steady-State Ocean Circulation Explorer (GOCE) missions have provided continuous and accurate accelerometer observations for the periods 2000–2010, 2002–2015, and 2009–2013, respectively. In addition, the accelerometers onboard each of the three Swarm satellites have been taking nongravitational measurements since November 2013. The higher spatial and temporal resolution provided by LEO accelerometers has revealed numerous intriguing features in the global distribution of thermospheric density, including the equatorial mass anomaly (EMA), the midnight density maximum (MDM), the geomagnetic cusp enhancements (GCEs), and traveling atmospheric disturbances [65].

Information from the acceleration in cross-track and radial directions can be used to derive measurements of thermospheric wind speed. First derivations of thermospheric winds can be found in [66], where the triaxial accelerometer measurements from the SETA instrument are analyzed. Sutton *et al.* [67] described two different approaches for density and wind derivation, and an improved iterative algorithm was developed in [68]. Recent publications on thermospheric wind variations can be found in, e.g., [69] and [70]. In principle, wind determination could be derived for the radial direction, but accurate instrument calibration, and radiation-pressure and lift-force-models are required.

C. Thermospheric Estimation From GNSS Measurements

In the recent years, several studies have shown that nongravitational accelerations, and derived neutral densities, can be estimated through GPS-based POD of LEO. First attempts were made in [71] and [72], where the authors estimated the nongravitational accelerations from CHAMP accelerometers by omitting the nongravitational force models in a highly reduced dynamic POD process. In this scheme, the GEODYN software was employed for all POD computations. GEODYN is based on a standard Bayesian weighted batch least squares estimator, where the piecewise linear functions are used to be computed at 10–15-min resolution for best results. In order to avoid a possible degraded quality at the edges, the orbits were processed in 30-h batches, with 3–6-h overlaps between subsequent orbits. Recent results of POD-based estimates from SWARM, GOCE, GRACE, and CHAMP have shown good agreement with the corresponding nongravitational accelerations [15], [73]–[75].

In the POD process, atmospheric densities can also be obtained as a correction to an atmospheric model. For instance, McLaughlin *et al.* [76] used a set of POE in a sequential orbit determination scheme to estimate thermospheric
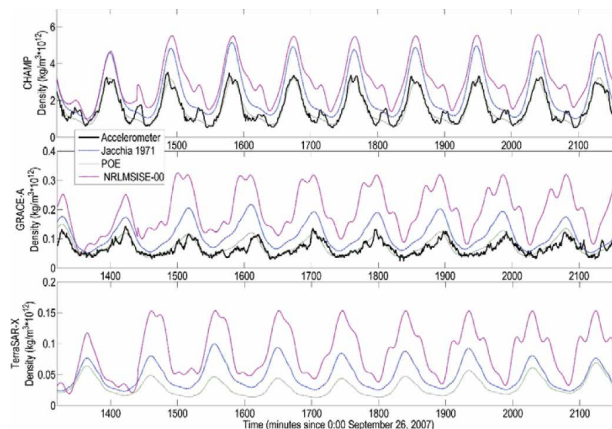

Fig. 6. *Measured, modeled, and POE-derived neutral densities from CHAMP, GRACE, and TerraSAR-X on September 26–27, 2007. ODTK software is used for POD [76].*

densities from GRACE, CHAMP, and TerraSAR-X. The Orbit Determination Tool Kit (ODTK) was employed for density estimation, where the authors input the POE in a sequential processing, filtering, and smoothing scheme to obtain time-variable densities and ballistic coefficients. Fig. 6 shows the measured, modeled, and POE-derived neutral densities from CHAMP and GRACE accelerometer and TerraSAR-X GNSS measurements on September 26–27, 2007 [76]. Results showed that POE-based densities were more accurate than the densities estimated from commonly used empirical models.

By applying all best available force models in multiple LEO, Kuang *et al.* [16] computed nongravitational accelerations and inferred thermospheric mass densities by estimating the stochastic accelerations that compensate for the dynamic model errors in the reduced-dynamic POD approach. Daily solutions were generated using orbit arcs of 30 h, with stochastic accelerations estimated from GPS ionosphere-free carrier phase and carrier-smoothed pseudorange measurements. Contrasting with the method of Ijssel *et al.* [71], both accuracy and resolution were improved because estimating accelerations to compensate for the model errors allows stronger stochastic constraints in the reduced-dynamic filtering. The authors identified useful data from CHAMP, GRACE-A/B, TerraSAR-X, and SAC-C.

The use of POD least squares estimators to derive density measurements can become a complex task, and recent studies [77], [17] have shown that nongravitational accelerations can also be derived from numerical differentiation of POE. Besides an unknown periodic systematic error identified in the POE solution, Calabia *et al.* [77] showed that the numerical differentiation requires an increment of time which minimizes the arc-to-chord error at a given threshold. Then, thermospheric mass densities inferred through numerical differentiation of POE have recently been investigated in [78]. In Fig. 7, the global averaged densities
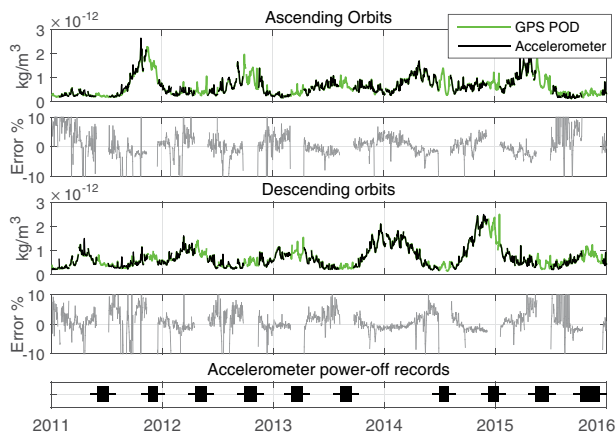
Fig. 7. *Global daily averaged densities and differences of relative errors between the POE-based and the accelerometer-based densities (2011–2016), i.e.. (POE-ACC)/ACC, separated in ascending orbits (top panels) and descending orbits (bottom panels). Accelerometer-based densities are plotted in black and GRACE GPS-POE estimates are plotted in green. The bottom timeline shows the days when accelerometer measurements were turned off due to power requirements [78].*

Fig. 8. *Thermospheric density variations fixed at Greenwich meridian, 475-km altitude, F10.7 = 80 sfu. From top to bottom, (a) in function of doy and latitude for 5, 11, 17, and 23 h LST, and (b) in function of LST and latitude for ME, JS, SE, and DS. From left to right, averaged accelerometer- and MSIS-based densities along GRACE orbits (raster plots), and direct calculations (contour plots) from [81].*

along descending and ascending orbits are plotted for both accelerometer- and POE-based techniques. The days when accelerometers were powered off are pictured in the bottom timeline graph. Taking accelerometer measurements as accurate reference, the relative errors for the GPS POE estimates are shown for both ascending and descending orbits. It can be seen that the maxima amplitude of the differences reaches up to 10%, mostly during low-density periods, and during low-density periods, the differences stay below 5% of the background density.

IV. THERMOSPHERIC VARIATIONS

A. Secular Thermospheric Density Variations

Thermospheric tides are mainly caused by the solar irradiations. LST is the largest secular variation, producing a clear density enhancement in the sunlit side of Earth. Geographically, two clear different structures can be recognized on the day and night sides. These include the EMA, which is a density minimum on the dayside, clearly aligned to the geomagnetic equator, and with two maxima at ±20° geomagnetic latitude [79], and the MDM, which is a midnight density maximum (instead of a minimum), around the equator, and with lower values (instead higher values) at middle latitudes [80]. The recent study by Calabia and Jin [81] has presented a clear understanding of global thermospheric mass density variations. For instance, Fig. 8 shows the thermospheric density variations derived from GRACE accelerometers and MSIS (fixed at Greenwich meridian and solar-flux conditions $F10.7 = 80$ sfu), in function of doy and latitude, for the scenarios of March equinox (ME), June solstice (JS), September equinox (SE), and
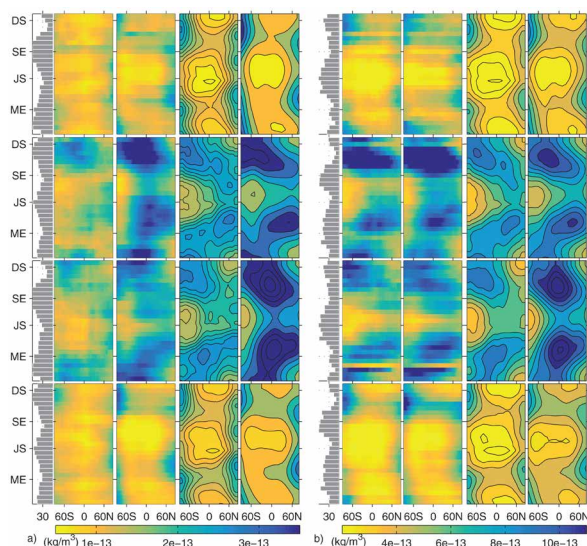
December solstice (DS), in function of DOY and latitude, for scenarios at 5, 11, 17, and 23 h LST. The latitudinal annual fluctuation following the subsolar point has shown two maxima peaks in June, and only one in December. In addition, a middle-latitude four-wave pattern has been found to have two maxima at 12 and 21 h LST and two minima at 1 and 17 h LST. In addition, Calabia and Jin [81] found strong contributions at the frequencies of the T, P, R, S, and K constituents of the theory of tides (radiational constituents), and additional periods at 83, 93, 152, and 431 day, which could be attributed to a long-term solar secular activity, and a possible free-core nutation coupling.

Besides solar irradiative tides, the effects of the Moon on Earth generate a secular variation in the thermosphere. First insights of the lunar atmospheric tide were made by Newton and studied by Laplace. Since then, many observational studies on solar and lunar atmospheric tides have been carried out. Comprehensive reviews can be found in [82] and [83]. Recently, Zhang *et al.* [84] suggested that at the altitude of CHAMP and GRACE, other factors are negligible compared with lunar atmospheric tide.

Finally, an important secular variation is produced by the variable surface of the Sun. Different sunspots provide different speeds and densities of solar wind which can form a spiral with outward fast-moving and slow-moving streams. Fast moving streams tend to overtake slower streams forming turbulent corotating interaction regions. Recurrent geomagnetic forcing related to CIR can produce density variations with a periodicity at subharmonics of the solar rotation period (~9 day, ~7 day, ~ 5 day). In addition, the rotational

variation of the Sun (~27 day) can produce secular appearances of bright regions (identified as solar plages), which are usually associated with sunspots.

Thermospheric variations during storms and CMEs are ejections of clouds of electrons, ions, and atoms through the corona of the Sun into space. In the thermosphere, CMEs increase the X-ray and EUV irradiance, causing immediate energy-absorption, ionization, and dissociation of molecules. CMEs are fast-moving bursts of plasma caused by release of magnetic energy at the Sun. CMEs and geomagnetic storms associated with CMEs can produce rapid thermospheric Joule heating and particle precipitation along Earth's magnetic field lines. This is a high latitude phenomenon which is mainly located in the auroral region. Shortly afterwards to these density enhancements in the auroral regions, the whole-globe thermosphere can respond with southward traveling gravity waves and a global increase of neutral mass density from several hours to several days.

For example, on March 17, 2013, the halo CME arrived at Earth and produced a moderate G2-level geomagnetic storm. Consequently, the energetic solar wind plasma with the favorable disposition of the interplanetary magnetic field produced thermospheric Joule heating and particle precipitation along Earth's magnetic field lines. During this period, the GRACE satellites were approximately located at 0 h LST and the corresponding +12 h for their complementary descending orbital leg. Fig. 9 shows the short-term
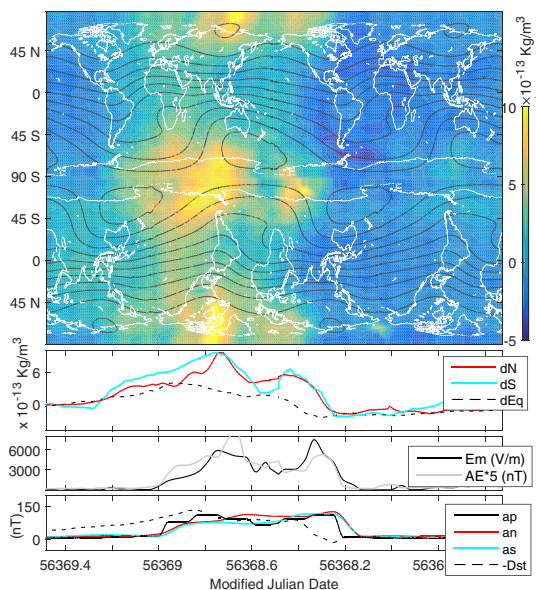
Fig. 10. *Density variations from GRACE accelerometer and NRLMSISE-00 normalized to 475 km [81].*

thermospheric density variations (free from local time and annual variations) inferred from GRACE GPS-POE during the moderate G2-level geomagnetic storm of March 16–17, 2013. In this figure, time evolution is defined from right to left (Earth rotation with respect to GRACE's orbital plane), and from bottom to top (satellite's along-track direction). Profiles at equator (dEq) and poles (dN, dS) are plotted together with the Em, AE, ap, an, and as space-weather and geomagnetic indices.

A clear example is the huge geomagnetic storm that occurred in March 2015 at equinox period, and under moderated solar-flux circumstances ($F10.7 \approx 120$ sfu). In that moment, the GRACE satellites were located at 6:25 h LST and the corresponding +12 h for the complementary orbital leg. Calabia and Jin [81] compared density estimates to the quiet-time surrounding period, and found that enhancements peaked at the cusp regions with absolute maxima deviation and maximum of mean latitudinal deviation above 500% and 180%, respectively. Figs. 10 and 11 show the MSIS model underestimates up to about 70% the mean magnitude and about 50% the diurnal amplitude. Later, the empirical model overestimates the mean value for a period of 48 h, up to about 170% of the accelerometer measurements [81]. It is clear that the NRLMSISE-00 empirical model is unable to reproduce most of the observed features, with smaller amplitudes and mean deviated values. In Fig. 11, mean-per-orbit GRACE values have been parameterized in terms of solar flux (F10.7), solar wind merging electric field (Em), and the geomagnetic Ap index. In this case, both Em and Ap

Fig. 9. *Short-term thermospheric density variations inferred from GRACE GPS-POE and its profiles at equator (dEq) and poles (dN, dS), plotted together with Em, AE, ap, an, and as, for the moderate G2-level geomagnetic storm of March 16–17, 2013 (from right to left and from bottom to top: March 16, 2013 12 h 36 m to March 18, 2013 11 h 35 m). GRACE's angle β' during this period is 173° (Sun to ascending leg). Accelerometer-based densities are not available due to instrument power-off during this month. The vertical magnetic field component (Z) is plotted in dashed–dotted lines [78].*
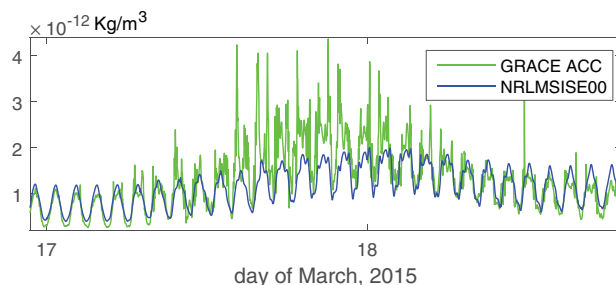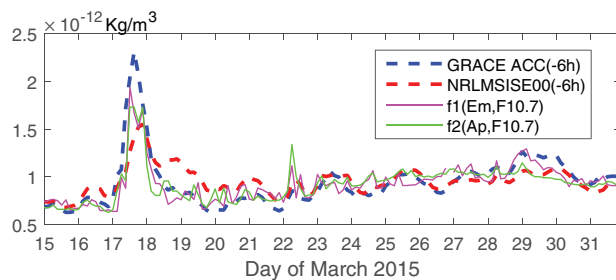
Fig. 11. *The mean values per orbit from GRACE, suggested parameterizations (f_1 and f_2), and the NRLMSISE-00 model for comparison [81].*

parameterizations from GRACE represent storm-time density variations better than NRLMSISE-00.

V. CHALLENGES AND PERSPECTIVE

In this review, we summarize past and present developments and efforts in sensing and modeling thermospheric density and wind variations as well as the scientific contribution of accelerometers and GNSS receivers on small LEO satellites. This is a valuable source of information for the thermosphere research community. Although the current Swarm and planned GRACE follow-on missions provide available accelerometer measurements throughout the next decade, the works presented in this review show that nongravitational accelerations and the thermospheric neutral densities can be also estimated through GNSS-based POD of LEO.

An important topic is the modeling of simultaneous satellite measurements in a combined solution of winds and densities. A clear example is given in Fig. 12, showing two simultaneous time series of density and cross winds of CHAMP and GOCE on April 5, 2010. Note that the intersection of different planes can reconstruct the 2-D horizontal wind vector 1-D crosswind measurements. The monitoring with multiple orbital planes can make possible a more complete study of density and wind variations as a function of LST and altitude.

It is clear that the recent advances in retrieving nongravitational accelerations and retrieving neutral density and winds through POD estimators require high technical knowledge and dedicated POD software (e.g., GEODYN, ODTK). However, with the increasing number of LEO satellites being equipped with high-precision GNSS receivers, and more enhanced data processing and orbit determination strategies, the feasible technique of determining thermospheric mass density variations through numerical differentiation of POE promises potentially good application. In addition, although previous studies have shown the ability to derive cross-track nongravitational accelerations from GNSS, the use of numerically differentiated accelerations to derive thermospheric winds is still a challenge.
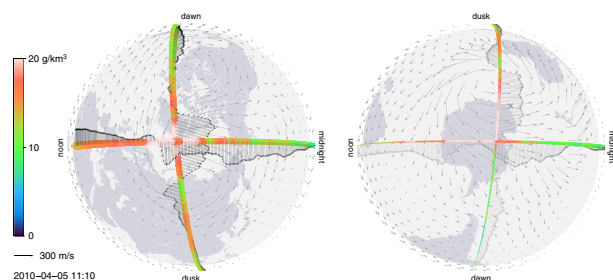

Fig. 12. *Density (color scale) and wind (arrows) data from both GOCE and CHAMP accelerometers, on April 5, 2010. Densities normalized to 300-km altitude. The background wind field is from the HWM07 model [69].*

The current force models could help to improve real-time maneuvers. For instance, it has been demonstrated [85] that the use of accurate solar radiation pressure and density and wind models could be employed to help attitude control and real-time maneuvers. This is a valuable contribution that would increase the lifetime of a LEO satellite. Since geomagnetic storms are considered a key in the ionosphere–thermosphere–magnetosphere system, the automatic detection of sudden commencements is also currently being investigated. Seen from the point of view of early control maneuvers and mission lifetime predictions, it is clear that the combination of sudden commencements of geomagnetic storms, with the real-time orbit determination of LEO [86] is a clear advance in LEO strategies.

The main source of ions for the ionosphere is originated by the photoabsorption, photoionization, and photodissociation of molecules through EUV solar radiation in the thermosphere, and energy transfer varies with LST, annual, and solar cycles. Variations in energy exchange from ions to neutrals produce the expansion/contraction of the thermosphere, and the consequent changes of neutrals density. Existing plasma is also transported vertically with the neutral medium, and horizontal neutral winds can move plasma along the magnetic field. The lower atmosphere transfers energy and the magnetosphere produces currents, joule heating, and electric fields. The present MIT models are unable to predict the variability as accurately and efficiently required, and the resulting processes from geomagnetic storms, CMEs, and solar wind (CMEs, shocks, high speed streams, high-intensity long-duration auroral activity) are still not well understood. Currently, the global nature of the observations can increase the understanding of the MIT system and, combining empirical with physical models, the understanding of all involved parameters and processes in the thermosphere is one of the challenges for the future.

With recent advances of new technologies and instruments, it can be employed to validate satellite-based density and wind measurements. For instance, through using the data set observed by Fabry–Perot interferometer, Liu *et al.* [87] have recently showed that thermospheric nighttime wind oscillations were different from that of thermospheric density, with meridional winds better correlating with both geomagnetic and solar-wind proxies than with solar-flux radiation. Zhang *et al.* [88] recently investigated the physical mechanism of the observed dayside high-latitude upper thermospheric from TIEGCM numerical simulations, validated their simulations with observations of the High altitude Interferometer WIND (HIWIND) balloon, and demonstrated that the model was capable to reproduce the unexpected afternoon equatorward thermospheric winds. Ion drag derived from the magnetospheric lobe cell convection is a probable reason for the unexpected wind change. Longitudinal structure is also influenced by several factors, including the chemical composition and the meridional winds at the altitude of the F region. England *et al.* [89]

used a new model of ionosphere (Sami2) to test the electrodynamic and chemical–dynamical coupling mechanisms. Siskind *et al.* [90] proposed that the decrease of O/N$_2$ ratio leads to a decrease in ionospheric electron density. He found an underestimation of peak electron density of the ionospheric F2 layer that was probably resulted from TIE-GCM uncertainties in the bottom boundary for atomic oxygen.

With the continuous technological advancement and the increasing knowledge on thermospheric processes, LEO satellites are constantly decreasing in altitude, size, and budget [91], and more experiments and new miniaturized instruments can be tested, e.g., the Broglio Drag Balance Instrument [92], or the miniaturized pressure gauge devices. Several other techniques could be included and integrated in thermosphere research and modeling in the future, including ultraviolet remote sensing, the incoherent scatter radar, and atmospheric occultation [93]. ∎

Acknowledgements

REFERENCES

[1] J. M. Forbes and R. G. Roble, "Thermosphere-ionosphere coupling: An experiment in interactive modeling," *J. Geophys. Res.*, vol. 95, no. A1, pp. 201–208, 1990.

[2] S. Y. Li and C. H. Liu, "Modeling the effects of ionospheric scintillations on LEO Satellite communications," *IEEE Commun. Lett.*, vol. 8, no. 3, pp. 147–149, Mar. 2004.

[3] S. G. Jin, J. Park, J. Wang, B. Choi, and P. Park, "Electron density profiles derived from ground-based GPS observations," *J. Navig.*, vol. 59, no. 3, pp. 395–401, 2006.

[4] S. G. Jin and J. Park, "GPS ionospheric tomography: A comparison with the IRI-2001 model over South Korea," *Earth Planets Space*, vol. 59, no. 4, pp. 287–292, 2007.

[5] S. G. Jin, O. F. Luo, and P. Park, "GPS observations of the ionospheric F2-layer behavior during the 20th November 2003 geomagnetic storm over South Korea," *J. Geodesy*, vol. 82, no. 12, pp. 883–892, 2008.

[6] T. F. Lechtenberg, C. A. McLaughlin, T. Locke, and D. Mysore, "Thermospheric density variations: Observability using precision satellite orbits and effects on orbit propagation," *Space Weather*, vol. 11, pp. 34–45, Jan. 2013.

[7] R. A. Gummow, "GIC effects on pipeline corrosion and corrosion control systems," *J. Atmos. Solar-Terrestrial Phys.*, vol. 64, no. 16, pp. 1755–1764, 2002.

[8] T. Molinski, "Geomagnetically induced currents: Causes, effect, and mitigation," *IEEE Can. Rev.*, vol. 13, 1996.

[9] J. G. Kappenman, "Geomagnetic storms and their impact on power systems," *IEEE Power Eng. Rev.*, vol. 16, no. 5, p. 5, May 1996.

[10] J. K. Owens, W. W. Vaughan, K. O. Niehuss, and J. Minow, "Space weather, earth's neutral upper atmosphere (thermosphere), and spacecraft orbital lifetime/dynamics," *IEEE Trans. Plasma Sci.*, vol. 28, no. 6, pp. 1920–1930, Jun. 2000.

[11] J. T. Emmert, "Thermospheric mass density: A review," *Adv. Space Res.*, vol. 56, no. 5, pp. 773–824, 2015.

[12] S. Bruinsma, D. Tamagnan, and R. Biancale, "Atmospheric densities derived from CHAMP/STAR accelerometer observations," *Planetary Space Sci.*, vol. 52, no. 4, pp. 297–312, 2004.

[13] E. Doornbos, "Thermospheric density and wind determination from satellite dynamics," Ph.D. dissertation, Delft Univ. Technol., Delft, The Netherlands, 2011.

[14] J. van den Ijssel and P. Visser, "Performance of GPS-based accelerometry: CHAMP and GRACE," *Adv. Space Res.*, vol. 39, no. 10, pp. 1597–1603, 2007.

[15] P. Visser, E. Doornbos, J. van den IJssel, and J. de Teixeira da Encarnação, "Thermospheric density and wind retrieval from Swarm observations," *Earth Planets Space*, vol. 65, p. 12, Nov. 2013.

[16] D. Kuang, S. Desai, A. Sibthorpe, and X. Pi, "Measuring atmospheric density using GPS–LEO tracking data," *Adv. Space Res.*, vol. 53, no. 2, pp. 243–256, 2014.

[17] A. Calabia and S. G. Jin, "GPS-based non-gravitational accelerations and accelerometer calibration," in *Satellite Positioning: Methods, Models and Applications*, S. Jin, Ed. Rijeka, Croatia: InTech, 2015, pp. 47–72.

[18] I. Harris and W. Priester, "Time-dependent structure of the upper atmosphere," *J. Atmos. Sci.*, vol. 19, no. 4, pp. 286–301, 1962.

[19] L. G. Jacchia, "Static diffusion models of the upper atmosphere with empirical temperature profiles," *Smithsonian Contrib. Astrophys.*, vol. 8, p. 215, 1964.

[20] B. R. Bowma *et al.*, "A new empirical thermospheric density model JB2008 using new solar and geomagnetic indices," in *Proc. AIAA/AAS Astrodyn. Specialist Conf. Exhib.*, Honolulu, HI, USA, Aug. 2008, pp. 18–21.

[21] F. Barlier, C. Berger, J. L. Falin, G. Kockarts, and G. Thuillier, "A thermospheric model based on satellite drag data," *Ann. de Geophys.*, vol. 34, no. 1, pp. 9–24, 1978.

[22] S. Bruinsma, "The DTM-2013 thermosphere model," *J. Space Weather Space Clim.*, vol. 5, p. A1, Feb. 2015.

[23] A. E. Hedin *et al.*, "A global thermospheric model based on mass spectrometer and incoherent scatter data MSIS. I—N2 density and temperature," *J. Geophys. Res.*, vol. 82, pp. 2139–2147, Jul. 1977.

[24] D. R. Bates, "Some problems concerning the terrestrial atmosphere above about the 100 km level," *Proc. Roy. Soc. A*, vol. 253, pp. 451–462, Dec. 1959.

[25] J. M. Picone, A. E. Hedin, D. P. Drob, and A. C. Aikin, "NRLMSISE-00 empirical model of the atmosphere: Statistical comparisons and scientific issues," *J. Geophys. Res.*, vol. 107, no. A12, p. 1468, 2002.

[26] F. A. Marcos, D. F. Gillette, and E. C. Robinson, "Evaluation of selected global thermospheric density models during low solar flux conditions," *Adv. Space Res.*, vol. 3, no. 1, pp. 85–89, 1983.

[27] J. T. Emmert, "Thermospheric mass density: A review," *Adv. Space Res.*, vol. 56, no. 5, pp. 773–824, 2015a.

[28] T. Hirano and S. Watanabe, "Empirical model of the thermospheric mass density based on CHAMP satellite observation," *J. Geophys. Res., Space Phys.*, vol. 118, no. 2, pp. 843–848, 2013.

[29] A. Calabia and S. G. Jin, "New modes and mechanisms of thermospheric mass density variations from GRACE accelerometers," *J. Geophys. Res. Space Phys.*, vol. 121, no. 11, 2016.

[30] J. O. Berheide, J. M. Forbes, X. Zhang, and S. L. Bruinsma, "Climatology of upward propagating diurnal and semidiurnal tides in the thermosphere," *J. Geophys. Res.*, vol. 116, p. A11306, Nov. 2011.

[31] D. P. Drob *et al.*, "An empirical model of the earth's horizontal wind fields: HWM07," *J. Geophys. Res.*, vol. 113, p. A12304, 2008.

[32] A. E. Hedin *et al.*, "Empirical wind model for the upper, middle and lower atmosphere," *J. Atmos. Sol. Terrestrial Phys.*, vol. 58, no. 13, pp. 1421–1447, 1996.

[33] D. P. Drob *et al.*, "An update to the horizontal wind model (HWM): The quiet time thermosphere," *Earth Space Sci.*, vol. 2, pp. 301–319, 2015.

[34] R. A. Akmaev, "Whole atmosphere modeling: Connecting terrestrial and space weather," *Rev. Geophys.*, vol. 49, p. RG4004, 2011.

[35] A. D. Richmond, E. C. Ridley, and R. G. Roble, "A thermosphere/ionosphere general circulation model with coupled electrodynamics," *Geophys. Res. Lett.*, vol. 19, no. 6, pp. 601–604, 1992.

[36] L. Qian *et al.*, "The NCAR TIE-GCM: A community model of the coupled thermosphere/ionosphere system," *Geophys. Monogr. Ser.*, vol. 201, pp. 73–83, 2014.

[37] J. S. Kim *et al.*, "Improvement of TIE-GCM thermospheric density predictions via incorporation of helium data from NRLMSISE-00," *J. Atmos. Sol.-Terr. Phys.*, vol. 77, pp. 19–25, Mar. 2012.

[38] M. E. Hagan, R. G. Roble, and J. Hackney, "Migrating thermospheric tides," *J. Geophys. Res. Atmos.*, vol. 106, no. 106, pp. 12739–12752, 2001.

[39] K. Häusler *et al.*, "Improved short-term variability in the thermosphere-ionospheremesosphere- electrodynamics general circulation model," *J. Geophys. Res. Space Phys.*, vol. 119, no. 8, pp. 6623–6630, 2014.

[40] C. J. Rice *et al.*, "Atmosphere Explorer pressure measurements: Ion gauge and capacitance manometer," *Radio Sci.*, vol. 8, no. 4, pp. 305–314, Apr. 1973.

[41] A. E. Hedin, "A revised thermospheric model based on mass spectrometer and incoherent scatter data: MSIS-83," *J. Geophys. Res.*, vol. 88, pp. 10170–10188, Dec. 1983.

[42] S. Chakrabarti, B. Bush, D. Cotton, G. R. Gladstone, R. Link, and T. W. Barbee, "Remote sensing of the thermosphere, plasmasphere, and exosphere," *IEEE Trans. Nucl. Sci.*, vol. 37, no. 3, pp. 1274–1279, Mar. 1990.

[43] W. Priester, M. Röemer, and H. Volland, "The physical behavior of the upper atmosphere deduced from satellite drag data," *Space Sci. Rev.*, vol. 6, no. 6, pp. 707–780, 1967.

[44] J. A. Burns, "Elementary derivation of the perturbation equations of celestial mechanics," *Amer. J. Phys.*, vol. 44, no. 10, pp. 944–949, 1976.

[45] D. King-Hele, "Satellite orbits in an atmosphere," in *Theory and Applications*. Houston, TX, USA: Blackie, 1987.

[46] J. T. Emmert, J. M. Picone, J. L. Lean, and S. H. Knowles, "Global change in the thermosphere: Compelling evidence of a secular decrease in density," *J. Geophys. Res.*, vol. 109, p. A02301, 2004.

[47] J. M. Picone, J. T. Emmert, and J. L. Lean, "Thermospheric densities derived from spacecraft orbits: Accurate processing of two-line element sets," *J. Geophys. Res.*, vol. 110, p. A03301, Mar. 2005.

[48] P. E. Zadunaisky, "Small perturbations on artificial satellites as an inverse problem," *IEEE Trans. Aerosp. Electron. Syst.*, vol. 39, no. 4, pp. 1270–1276, Apr. 2003.

[49] B. D. Tapley, B. E. Schutz, and G. H. Born, *Statistical Orbit Determination*. San Diego, CA, USA: Academic, 2004.

[50] S. C. Wu, T. P. Yunck, and C. L. Thornton, "Reduced-dynamic technique for precise orbit determination of low earth satellites," *J Guid. Control Dyn.*, vol. 14, no. 1, pp. 24–30, 1991.

[51] O. Montenbruck and E. Gill, *Satellite Orbits: Models, Methods and Applications*. Berlin, Germany: Springer-Verlag, 2013.

[52] S. B. Luthcke, J. A. Marshall, S. C. Rowton, K. E. Rachlin, C. M. Cox, and R. G. Williamson, "Enhanced radiative force modeling of the tracking and data relay satellites," *J. Astron. Sci.*, vol. 45, no. 3, pp. 349–370, 1997.

[53] P. Knocke and J. Ries, "*Earth radiation pressure effects on satellites*," Center Space Res., Univ. Texas Austin, Austin, TX, USA, Tech. Memo. CSR-TM-87-01, 1987.

[54] E. K. Sutton, "Effects of solar disturbances on the thermosphere densities and winds from CHAMP and GRACE satellite accelerometer data," Ph.D. dissertation, Univ. Colorado, Boulder, CO, USA, 2008.

[55] R. A. Schamberg, "new analytic representation of surface interaction for hyperthermal free molecular flow," Rand Corp., Santa Monica, CA, USA, Tech. Rep. TR RM-2313, 1959.

[56] L. H. Sentman, "Free Molecule Flow Theory and its Application to the Determination of Aerodynamic Forces," Lockheed Missile Space Co., Sunnyvale, CA, USA, Tech. Rep. TR LMSC-448514, 1961.

[57] G. E. Cook, "Satellite drag coefficients," *Planetary Space Sci.*, vol. 13, no. 10, pp. 929–946, 1965.

[58] F. O. Goodman, *Fourth International Symposium on Rarefied Gas Dynamics*. New York, NY, USA: Academic, 1964.

[59] P. M. Mehta, C. A. McLaughlin, and E. K. Sutton, "Drag coefficient modeling for grace using direct simulation Monte Carlo," *Adv. Space Res.*, vol. 52, no. 12, pp. 2035–2051, 2013.

[60] P. M. Mehta *et al.*, "Comparing physical drag coefficients computed using different gas–surface interaction models," *J. Spacecraft Rockets*, vol. 51, no. 3, pp. 873–883, 2014.

[61] S. Rentz and H. Lühr, "Climatology of the cusp-related thermospheric mass density anomaly, as derived from CHAMP observations," *Ann. Geophys.*, vol. 26, pp. 2807–2823, 2008.

[62] S. Bruinsma, J. M. Forbes, R. S. Nerem, and X. Zhang, "Thermosphere density response to the 20–21 November 2003 solar and geomagnetic storm from CHAMP and GRACE accelerometer data," *J. Geophys. Res.*, vol. 111, p. A06303, Jan. 2006.

[63] C. Hwang, T. J. Lin, T. P. Tseng, and B. F. Chao, "Modeling orbit dynamics of FORMOSAT-3/COSMIC satellites for recovery of temporal gravity variations," *IEEE Trans. Geosci. Remote Sens.*, vol. 46, no. 11, pp. 3412–3423, Nov. 2008.

[64] E. Canuto, A. Molano, and L. Massotti, "Drag-free control of the GOCE satellite: Noise and observer design," *IEEE Trans. Control Syst. Technol.*, vol. 18, no. 2, pp. 501–509, Feb. 2010.

[65] J. T. Emmert, "Altitude and solar activity dependence of 1967-2005 thermospheric density trends derived from orbital drag," *J. Geophys. Res. Space Phys.*, vol. 120, no. 4, pp. 2940–2950, 2015.

[66] F. A. Marcos and J. M. Forbes, "Thermospheric winds from the satellite electrostatic triaxial accelerometer system," *J. Geophys. Res.*, vol. 90, pp. 6543–6552, Jul. 1985.

[67] E. K. Sutton, R. S. Nerem, and J. M. Forbes, "Density and winds in the thermosphere deduced from accelerometer data," *J. Spacecraft Rockets*, vol. 44, no. 6, pp. 1210–1219, 2007.

[68] E. Doornbos, J. van den IJssel, H. Lühr, M. Förster, and G. Koppen-wallner, "Neutral density and cross-wind determination from arbitrarily oriented multiaxis accelerometers on satellites," *J. Spacecraft Rockets*, vol. 47, no. 4, pp. 580–589, 2010.

[69] E. Doornbos *et al.*, "GOCE+ theme 3: Air density and wind retrieval using GOCE data," Delft Univ. Technol., Delft, The Netherlands, Tech. Rep., 2014.

[70] R. Lieberman, A. Akmaev, T. Fuller-Rowell, and E. Doornbos, "Thermospheric zonal mean winds and tides revealed by CHAMP," *Geophys. Res. Lett.*, vol. 40, pp. 2439–2443, 2013.

[71] J. van den IJssel, P. Visser, and R. Haagmans, "Determination of non-conservative accelerations from orbit analysis," in *Earth Observation with CHAMP Results from Three Years in Orbit*, C. Reigber, H. Luhr, P. Schwintzer, and J. Wickert, Eds. New York, NY, USA: Springer-Verlag, 2004, pp. 95–100.

[72] J. van den Ijssel and P. Visser, "Determination of non-gravitational accelerations from GPS satellite-to-satellite tracking of CHAMP," *Adv. Space Res.*, vol. 36, no. 3, pp. 418–423, 2005.

[73] C. Siemes *et al.*, "Swarm accelerometer data processing from raw accelerations to thermospheric neutral densities," *Earth Planet Space*, vol. 68, p. 92, Dec. 2016.

[74] J. van den Ijssel, "GPS-based precise orbit determination and accelerometry for low flying satellites," Ph.D. dissertation, Delft Univ. Technol., Delft, The Netherlands, 2014.

[75] E. Doornbos, P. Visser, G. Koppenwallner, and S. Fritsche, "GOCE+ theme 3: Air density and wind retrieval using GOCE data," Delft Univ. Technol., Delft, The Netherlands, Tech. Rep. ESA AO/1-6367/10/NL/AF, 2014.

[76] C. A. McLaughlin, T. Lechtenberg, E. Fattig, and D. Mysore Krishna, "Estimating density using precision satellite orbits from multiple satellites," *J. Astron. Sci.*, vol. 59, nos. 1–2, pp. 84–100, 2013.

[77] A. Calabia, S.G. Jin and R. Tenzer, "A new GPS-based calibration of GRACE accelerometers using the arc-to-chord threshold uncovered sinusoidal disturbing signal," *Aerospace Sci. Technol.*, vol. 45, pp. 265–271, 2015.

[78] A. Calabia and S. G. Jin, "Thermospheric density estimation and responses to the March 2013 geomagnetic storm from GRACE GPS-determined precise orbits," *J. Atmos. Sol.-Terr. Phys.*, vol. 154, pp. 167–179, 2017.

[79] H. Liu, H. Lühr, and S. Watanabe, "Climatology of the equatorial thermospheric mass density anomaly," *J. Geophys. Res.*, vol. 112, p. A05305, May 2007.

[80] R. Ma *et al.*, "Variations of the nighttime thermospheric mass density at low and middle latitudes," *J. Geophys. Res.*, vol. 115, p. A12301, Dec. 2010.

[81] A. Calabia and S. G. Jin, "Thermospheric mass density variations during the March 2015 geomagnetic storm from GRACE accelerometers," in *Proc. Prog. Electromagn. Res. Symp.*, Shanghai, China, Aug. 2016, pp. 4976–4980.

[82] S. Chapman and R. S. Lindzen, *Atmospheric Tides: Thermal and Gravitational*. New York, NY, USA: Gordon Breach, 1970.

[83] J. M. Forbes and H. B. Garrett, "Theoretical studies of atmospheric tides," *Rev. Geophys.*, vol. 17, no. 8, pp. 1951–1981, 1979.

[84] J. T. Zhang, J. M. Forbes, C. H. Zhang, E. Doornbos, and S. L. Bruinsma, "Lunar tide contribution to thermosphere weather," *Space Weather*, vol. 12, no. 8, pp. 538–551, 2014.

[85] S. N. Singh and W. Yim, "Nonlinear adaptive spacecraft attitude control using solar radiation pressure," *IEEE Trans. Aerosp. Electron. Syst.*, vol. 41, no. 3, pp. 770–779, Mar. 2005.

[86] Y. Yang, X. Yue, and A. G. Dempster, "GPS-based onboard real-time orbit determination for LEO satellites using consider Kalman filter," *IEEE Trans. Aerosp. Electron. Syst.*, vol. 52, no. 2, pp. 769–777, Feb. 2016.

[87] X. Liu, J. Xu, S.-R. Zhang, Q. Zhou, and W. Yuan, "Solar activity dependency of multiday oscillations in the nighttime thermospheric winds observed by Fabry-Perot interferometer," *J. Geophys. Res. Space Phys.*, vol. 120, pp. 5871–5881, 2015.

[88] B., Zhang, W. Wang, and Q. Wu, "Effects of magnetospheric lobe cell convection on dayside upper thermospheric winds at high latitudes," *Geophys. Res. Lett.*, vol. 43, pp. 8348–8355, 2016.

[89] S. L. England *et al.*, "Modeling of multiple effects of atmospheric tides on the ionosphere: An examination of possible coupling mechanisms responsible for the longitudinal structure of the equatorial ionosphere," *J. Geophys. Res.*, vol. 115, p. A05308, 2010.

[90] D. E. Siskind *et al.*, "Simulations of the effects of vertical transport on the thermosphere and ionosphere using two coupled models," *J. Geophys. Res. Space Phys.*, vol. 119, pp. 1172–1185, 2014.

[91] R. Li *et al.*, "Thermospheric mass density derived from CHAMP satellite precise orbit determination data based on energy balance method," *Sci. China Earth Sci.*, vol. 60, no. 8, pp. 1495–1506, 2017.

[92] F. Santoni, F. Iergentili, and F. Graziani, "Broglio Drag Balance for neutral thermosphere density measurement on UNICubeSAT," *Adv. Space Res.*, vol. 45, no. 5, pp. 651–660, 2010.

[93] X. Zhao *et al.*, "Evaluation of regional ionospheric grid model over China from dense GPS observations," *Geod. Geodyn.*, vol. 7, no. 5, pp. 361-368, 2016.

ABOUT THE AUTHORS

Shuanggen Jin received the B.Sc. degree in geodesy from Wuhan University, Wuhan, China, in 1999 and the Ph.D. degree in geodesy from the University of Chinese Academy of Sciences, Beijing, China, in 2003.

He is a Professor at Shanghai Astronomical Observatory, Chinese Academy of Sciences (CAS), Shanghai, China and Academician at Russian Academy of Natural Sciences, Moscow, Russia. His main research areas include satellite navigation, space geodesy, remote sensing, climate change, geophysics, and planetary sciences. He published over 400 papers in international peer-reviewed journals and conference proceedings, holds eight patents/software copyrights and wrote eight books/monographs with more than 3200 citations and H-index>35.

Prof. Jin was President of the International Association of CPGPS (2016–2017) and of the International Association of Planetary Sciences (IAPS) (2013–2017). He is Chair of IUGG Union Commission on Planetary Sciences (UCPS) (2015–2019); Editor-in-Chief of the *International Journal of Geosciences* (since 2010); an Associate Editor of the IEEE Transactions on Geoscience and Remote Sensing (since 2014), *Journal of Navigation* (since 2014), and *Advances in Space Research* (2013–2017); and an Editorial Board member of *Remote Sensing* (since 2017), *GPS Solutions* (since 2016), *Journal of Geodynamics* (since 2014), and *Planetary and Space Science* (since 2014). He received one First-class and four Second-class Prizes of Provincial Awards and the Fu Chengyi Youth Science & Technology Award (2012), has been listed in the 100-Talent Program of CAS (2010), and has been a Fellow of the International Association of Geodesy (IAG) since 2011.

Andrés Calabia (Member, IEEE) is currently working toward the Ph.D. degree at Shanghai Astronomical Observatory, Chinese Academy of Sciences (CAS), Shanghai, China.

He has over five years' experience in academic research, and about seven years' experience in industry. He is highly skilled in geodesy, navigation, and remote sensing, with a broad range of analytic techniques, including data analysis and algorithm development.

Liangliang Yuan is currently working toward the M.S. degree at Shanghai Astronomical Observatory, Chinese Academy of Sciences (CAS), Shanghai, China.

His main research areas are space geodesy, orbit determination aerospace science, and space science.